Phase-resolved magnetomotive OCT for imaging nanomolar concentrations of magnetic nanoparticles in tissues

Amy L. Oldenburg,[1,2,3] Vasilica Crecea,[2,4]
Stephanie A. Rinne,[2] and Stephen A. Boppart[1,2,5,*]

[1]*Department of Electrical and Computer Engineering, University of Illinois at Urbana-Champaign,*
1406 W. Green St., Urbana, IL 61801, USA
[2]*Beckman Institute for Advanced Science and Technology, University of Illinois at Urbana-Champaign,*
405 N. Mathews Ave., Urbana, IL 61801, USA
[3]*Current address: Department of Physics and Astronomy, University of North Carolina, Chapel Hill, NC 27599-*
3255, USA
[4]*Department of Physics, University of Illinois at Urbana-Champaign, 1110 W. Green St., Urbana, IL 61801, USA*
[5]*Mills Breast Cancer Institute, Carle Foundation Hospital,*
611 W. Park St., Urbana, IL 61801, USA
[*]*Corresponding author: boppart@uiuc.edu*

Abstract: Magnetic nanoparticles (MNPs) are increasingly important in magnetic resonance and biomedical optical imaging. We describe a method for imaging MNPs by detecting nanoscale displacements using a phase-resolved spectral-domain optical coherence tomography (OCT) system. Biological tissues and phantoms are exposed to ~800 G magnetic fields modulated at 56 and 100 Hz to mechanically actuate embedded iron oxide MNPs (~20 nm diameter). Sensitivity to 27 µg/g (~2 nM) MNPs within tissue phantoms is achieved by filtering paramagnetic from diamagnetic vibrations. We demonstrate biological feasibility by imaging topically applied MNPs during their diffusion into an excised rat tumor over a 2 hour time period.

©2008 Optical Society of America

OCIS codes: (170.4500) Optical coherence tomography; (170.3880) Medical and biological imaging; (160.3820) Magneto-optical materials.

References and links

1. J. F. Schenck, "Physical interactions of static magnetic fields with living tissues," Prog. Biophys. Mol. Biol. **87**, 185-204 (2005).
2. H. Watarai and M. Namba, "Capillary magnetophoresis of human blood cells and their magnetophoretic trapping in a flow system," J. Chromatogr. A **961**, 3-8 (2002).
3. M. Arruebo, R. Fernandez-Pachaco, M. R. Ibarra, and J. Santamaria, "Magnetic nanoparticles for drug delivery," Nano Today **2**, 22-32 (2007).
4. A. Ito, M. Shinkai, H. Honda, and T. Kobayashi, "Medical application of functionalized magnetic nanoparticles," J. Biosci. Bioeng. **100**, 1-11 (2005).
5. J. Dobson, "Magnetic nanoparticles for drug delivery," Drug Dev. Res. **67**, 66-60 (2006).
6. J.-H. Lee, Y.-M. Huh, Y.-W. Jun, J.-W. Seo, J.-T. Jang, H.-T. Song, S. Kim, E.-J. Cho, H.-G. Yoon, J.-S. Suh and J. Cheon, "Artificially engineered magnetic nanoparticles for ultra-sensitive molecular imaging," Nat. Med. **13**, 95-99 (2007).
7. D. E. Sosnovik and R. Weissleder, "Emerging concepts in molecular MRI," Curr. Opin. Biotechnol. **18**, 4-10 (2007).
8. D. Huang, E. A. Swanson, C. P. Lin, J. S. Schuman, W. G. Stinson, W. Chang, M. R. Hee, T. Flotte, K. Gregory, C. A. Puliafito, and J. G. Fujimoto, "Optical coherence tomography," Science **254**, 1178 (1991).
9. S. A. Boppart, A. L. Oldenburg, C. Xu, and D. L. Marks, "Optical probes and techniques for molecular contrast enhancement in coherence imaging," J. Biomed. Opt. **10**, 041208 (2005).
10. B. E. Applegate and J. A. Izatt, "Molecular imaging of endogenous and exogenous chromophores using ground state recovery pump-probe optical coherence tomography," Opt. Express **14**, 9142-9155 (2006).
11. H. Cang, T. Sun, Z.-Y. Li, J. Chen, B. J. Wiley, Y. Xia, and X. Li, "Gold nanocages as contrast agents for spectroscopic optical coherence tomography," Opt. Lett. **30**, 3048-3050 (2005).

12. A. Agrawal, S. Huang, A. W. H. Lin, M.-H. Lee, J. K .Barton, R. A. Drezek, and T. J. Pfefer, "Quantitative evaluation of optical coherence tomography signal enhancement with gold nanoshells," J. Biomed. Opt. **11**, 041121 (2006).
13. A. L. Oldenburg, M. H. Hansen, D. A. Zweifel, A. Wei, and S. A. Boppart, "Plasmon-resonant gold nanorods as low backscattering albedo contrast agents for optical coherence tomography," Opt. Express **14**, 6724-6738 (2006).
14. D. C. Adler, S.-W. Huang, R. Huber, and J. G. Fujimoto, "Photothermal detection of gold nanoparticles using phase-sentivie optical coherence tomography," Opt. Express **16**, 4376-4393 (2008).
15. J. N. Anker and R. Kopelman, "Magnetically modulated optical nanoprobes," Appl. Phys. Lett. **82**, 1102-1104 (2003).
16. J. S. Aaron, J. Oh, T. A. Larson, S. Kumar, T. E. Milner, and K. V. Sokolov, "Increased optical contrast in imaging of epidermal growth factor receptor using magnetically actuated hybrid gold/iron oxide nanoparticles," Opt. Express **14**, 12930-12943 (2006).
17. A. L. Oldenburg, J. R. Gunther, and S. A. Boppart, "Imaging magnetically labeled cells with magnetomotive optical coherence tomography," Opt. Lett. **30**, 747-749 (2005).
18. A. L. Oldenburg, F. Jean-Jacques Toublan, K. S. Suslick, A. Wei, and S. A. Boppart, "Magnetomotive contrast for *in vivo* optical coherence tomography," Opt. Express **13**, 6597-6614 (2005).
19. M. A. Choma, A. K .Ellerbee, C. Yang, T. L. Creazzo, J. A. Izatt, "Spectral-domain phase microscopy," Opt. Lett. **30**, 1162-1164 (2005).
20. J. Oh, M. D. Feldman, J. Kim, H. W. Kang, P. Sanghi, and T. E. Milner, "Magneto-motive detection of tissue-based macrophages by differential phase optical coherence tomography," Lasers Surg. Med. **39**, 266-272 (2007).
21. M. M. Chan, W. Lu, F. M. Merchant, J. D. Iglehart, and P. L. Miron, "Gene expression profiling of NMU-induced rat mammary tumors: cross species comparison with human breast cancer," Carcinogenesis **26**, 1343-1353 (2005).
22. B. H. Park, M. C. Pierce, B. Cense, S.-H. Yun, G. Mujat, G. J. Tearney, B. E. Bouma, and J. F. deBoer, "Real-time fiber-based multi-functional spectral-domain optical coherence tomography at 1.3 µm," Opt. Express **11**, 3931-3944 (2005).
23. A. L. Oldenburg, W. Luo, and S. A. Boppart, "High-resolution *in vivo* nanoparticle imaging using magnetomotive optical coherence tomography," Proc. SPIE **6097**, doi 10.1117/12.643609 (2006).
24. T. S. Ralston, D. L. Marks, P. S. Carney, and S. A. Boppart, "Interferometric synthetic aperture microscopy," Nat. Phys. **3**, 129-134 (2007).
25. A. M. Zysk, E. J. Chaney, and S. A. Boppart, "Refractive index of carcinogen-induced rat mammary tumours," Phys. Med. Biol. **51**, 2165-2177 (2006).
26. J. Zhang, J. S. Nelson, and Z. Chen, "Removal of a mirror image and enhancement of the signal-to-noise ratio in Fourier-domain optical coherence tomography using an electro-optic phase modulator," Opt. Lett. **30**, 147-149 (2005).
27. S. Makita, Y. Hong, M. Yamanari, T. Yatagai, and Y. Yasuno, "Optical coherence angiography," Opt. Express **14**, 7821-7840 (2006).

1. Introduction

Magnetic nanoparticles (MNPs) composed of biocompatible iron oxides (magnetite, Fe_3O_4, or maghemite, γ-Fe_2O_3) exhibit magnetic susceptibilities χ that are typically $>10^5$ times larger than that of human tissue, including red blood cells [1,2]. Not surprisingly, this fact has led to the increasing development of MNP-related technologies in biology and medicine [3]. Heating of MNPs with high frequency magnetic fields is being investigated as a possible cancer treatment by inducing hyperthermia in tumors [4]. Concentrating MNPs within disease sites may be accomplished using magnetic field gradients to pull them within the body [5]. Molecular-based targeting has been demonstrated with antibody-conjugated MNPs which accumulate within mammary tumors in an animal model [6]. MNPs have even been used for stratifying cell layers in tissue engineering [4]. The ability to monitor the targeting and therapy of MNPs has therefore become increasingly important in biomedicine, which has been particularly successful in magnetic resonance (MR) imaging where MNPs are contrast agents [7]. The availability of new imaging techniques appropriate to the microscale such as optical coherence tomography (OCT) can elucidate processes such as diffusion, active transport processes, and in general, biodistribution and kinetics, which may be currently limiting our ability to target MNPs [3].

Optical coherence tomography is a three-dimensional microstructural biomedical imaging modality that utilizes the coherence property of light to optically range light scattering structures [8]. Various types of contrast agents have been developed for OCT which may enhance its biomedical utility by enabling molecular imaging [9,10]. The use of plasmon-

resonant nanoparticles in OCT has been of particular interest as they exhibit extremely high optical scattering or absorption cross-sections [11-13]. Recently, a modulated OCT contrast method using plasmon-resonant nanoshells was demonstrated using the resonant photothermal heating of nanoshells to modulate the local refractive index [14]. Modulated OCT contrast is important to successfully achieve background rejection in highly scattering tissues. However, this method may be limited by cumulative heating in the tissue, and has yet to be demonstrated in a biological sample.

MNPs can be mechanically actuated with an externally applied magnetic field gradient, and novel magneto-optical particles have been designed for contrast in optical microscopy [15,16]. Magnetomotive OCT (MMOCT) is accomplished using an electromagnet which modulates a magnetic field within the tissue during OCT imaging [17]. This provides a mechanical displacement at the locations of MNPs in the tissue, which is observed as a shift in the OCT interferogram. MMOCT was first demonstrated in a cell scaffold containing a mixture of microparticle-labeled and unlabeled macrophage cells [17]. More recently, imaging of MNPs in the digestive tract of an *in vivo* African frog tadpole was shown [18]. Rejection of physiological motion for *in vivo* imaging was accomplished by acquiring two successive axial scans with the magnetic field off and a third with the field on, and comparing the signal changes between the on and off scans (magnetomotion) with those between the two off scans (physiological motion). However, these studies only tracked the amplitude of the OCT interference signal.

The use of optical phase to obtain sub-wavelength displacement sensitivity is very powerful for imaging biological samples [19]. A differential-phase OCT system was recently used to detect (but not image) the magnetomotion of MNP-laden macrophages in an animal model [20]. In the work described here, we present a new MMOCT system using a spectral-domain OCT system which provides sufficient phase sensitivity for phase-resolved imaging. Because it takes time for tissue to mechanically relax, the previous method of acquiring 3 successive axial scans in each location is not feasible if faster imaging times are required, such as for three-dimensional *in vivo* imaging. Therefore, in this system, the magnetic gradient force is modulated sinusoidally during a B-mode image frame, and background rejection is accomplished by acquiring an *a priori* image frame with the magnetic field off. To demonstrate biological relevance, we image the diffusion of MNPs into excised tumors from a rat model for human breast cancer; this model has been shown to be most similar to estrogen receptor-positive ductal carcinomas [21].

2. Theory

In this section, we will first describe the basis for mechanical motion of MNPs in biological media and how magnetomotion is driven in our system. Then we will explain how OCT is used to detect this motion, and how the data is collected and processed to produce images with magnetomotive contrast.

2.1 Magnetomotion in biological tissues

In our MMOCT system the magnetic field is applied using a solenoid, and imaging is performed on the sample immediately below the solenoid bore. By allowing the beam to pass through the central bore, *in vivo* imaging and imaging of thick tissues is possible, unlike other geometries [20] that use a central ferrite tip to concentrate the magnetic field gradient. Our geometry is such that, within the imaging volume, the radial components of the magnetic field are negligible and the magnetic field gradient is dominantly in the axial direction. In the following analysis we will therefore neglect the radial components and write forces F, magnetic fields B, and magnetizations M as one-dimensional entities which are essentially the axial (z) components of their true vector forms.

The force F_p on an MNP with volume V_p and volume magnetization M_p arising from an applied magnetic field B with a gradient along z can be written as:

$$F_p(z) = V_p M_p(B(z)) \frac{\partial B(z)}{\partial z} . \tag{1}$$

We assume for simplicity that the magnetic field is unmodified by the magnetization within the sample ($B=\mu_0 H$), and that the magnetic field does not fall off appreciably within our imaging depth ($B(z)=B(0)$). Analogous to Eq. (1), the tissue medium also experiences a force depending on its volume magnetization M_m and volume V_m. Thus, the net force F_{tot} on a tissue volume element V with embedded MNPs of number density N_p can be written:

$$F_{tot} = \left[(N_p V) V_p M_p(B) + V M_m(B) \right] \frac{\partial B}{\partial z} , \tag{2}$$

assuming the MNPs occupy a small fractional volume so that $V \approx V_m$. The response from human tissue is typically diamagnetic [1], so that M_m will have a sign opposite to that of the superparamagnetic MNPs M_p. Thus, there is a certain "critical" particle volume density ρ_{crit} at which the force from the MNPs exactly balances the opposing force from the tissue (F_{tot}=0):

$$\rho_{crit}(B) = N_p V_p = \frac{-M_m(B)}{M_p(B)} . \tag{3}$$

We note that this equation looks the same when written in terms of a mass density and mass magnetization. Therefore, when the tissue is loaded with an MNP concentration greater than ρ_{crit}, its net response will appear paramagnetic (motion toward $B \cdot \partial B / \partial z$), and for concentrations less than ρ_{crit} its motion will appear diamagnetic. As we will discuss below, discriminating the overall direction of motion (diamagnetic vs. paramagnetic) can improve the sensitivity of an MMOCT system.

For a weakly magnetic medium, M_m is linear in B for B less than several Tesla. However, MNPs reach saturation at sub-Tesla magnetic fields, so M_p is more accurately described by the Langevin function. This saturation in the denominator of Eq. (3) results in an increasing critical nanoparticle density ρ_{crit} with increasing B, as shown in Fig. 1. For magnetic fields sufficiently below saturation (less than ~500 G for our MNPs), $M_p(B)$ is still linear, and ρ_{crit} is near its minimum value of ~8 µg/g in silicone-based tissue phantoms.

In this regime of low B, the F_p from Eq. (1) is proportional to the square of the applied magnetic field B. Therefore, in order to induce a temporally modulated force that is a pure sinusoid, we chose to drive our electromagnet with the following voltage waveform $V(t)$:

$$V(t) = V_0 \sqrt{\frac{\sin(2\pi f_B t) + 1}{2}} , \tag{4}$$

where f_B is the modulation frequency, V_0 is the peak voltage, and $B(t)$ is linearly proportional to $V(t)$ (with negligible inductance for $f_B < 10$kHz). The offset is chosen to allow for the use of a unipolar power supply, which can be helpful when driving high currents. If the induced forces are sufficiently small, the system responds mechanically in a linear (Hookean) way such that the displacement $\Delta z(t)$ can be written:

$$\Delta z(t) = A \left(\frac{\sin(2\pi f_B t + \varphi) + 1}{2} \right) , \tag{5}$$

where A is the maximum amplitude of the displacement and φ is the mechanical phase lag. The amplitude A will be determined by F_{tot} which is linear in the concentration of MNPs according to Eq. (2), and also by the viscoelastic properties of the medium. Previous data suggests that A is linear with respect to the MNP concentration [18]. Thus, A can be used as a relative metric of MNP concentration. If the viscosity of the medium can be ignored, the value of φ will equal zero for a paramagnetic system (aligned motion) and π for a diamagnetic system (opposed motion). However, even in media with significant viscosity, one would expect to observe a shift of π when comparing para- and dia-magnetic media. In this way φ can be used to determine the direction of F_{tot}.

From the measured mechanical phase lag φ for a position in the tissue $\vec{r}$, we can design a normalized cosine filter $\hat{f}$ which suppresses diamagnetic signals as follows:

$$\hat{f}(\vec{r}) = \left(\frac{\cos(\varphi(\vec{r})) + 1}{2} \right). \tag{6}$$

This filter is multiplied pointwise with the magnetomotive signal at each pixel in order to select the locations in the image exhibiting paramagnetic motion. It will be applied in the following subsection.

Finally, this all can be related to a minimum detectible concentration of MNPs, ρ_{min}. We define ρ_{min} as that required to achieve a certain minimum MNP displacement amplitude A_{min} in order to overcome the OCT system hardware noise. In a Hookean system where A is proportional to F_{tot}, we can solve for ρ_{min} using Eqs. (1)-(3) as follows:

$$\rho_{min}(B) = \rho_{crit}(B) + c \frac{V_p A_{min} E_m}{F_p(B)} ,$$
$$= \rho_{crit}(B) + \rho_{noise}(B) \tag{7}$$

where E_m is an effective dynamic modulus of the medium at f_B which takes into account the viscoelastic properties of the relevant region around the imaging volume, c is a scaling factor depending on the geometry of the sample and magnetic field, and ρ_{noise} is the additional MNP concentration needed to detect magnetomotion above the OCT system noise. ρ_{noise} is inversely proportional to the force on the particles F_p. It is plotted in Fig. 1 for our MNPs, where the scaling factor $A_{min} E_m$ has been estimated based on our experimental results in Section 4. The resulting estimate of ρ_{min} is also shown in Fig. 1. We see that the optimum choice of B (that which minimizes ρ_{min}) is a tradeoff between a sufficiently low B to not saturate the MNPs and keep the motion paramagnetic (reducing ρ_{crit}), but sufficiently high B to induce enough force to displace the MNPs (reducing ρ_{noise}). This choice is both OCT system- and sample-dependent. We note that this analysis is performed for homogeneous tissue phantoms; inhomogeneous media such as a subvolume of MNPs within the imaging region may require a higher ρ_{min}.
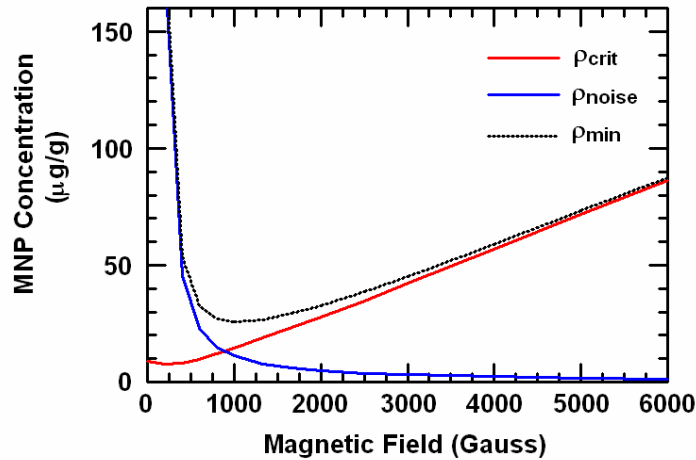

Fig. 1. Theoretical MNP densities ρ_{crit}, ρ_{noise}, and ρ_{min} according to Eqs. (3) and (7). SQUID magnetometry measurements of the MNPs and tissue phantom silicone medium were used to generate the curves. The unknown scaling factor for ρ_{noise} was estimated from the experimental results.

What is the sensitivity in the case where the mechanical phase filter (Eq. (6)) is not used to discriminate paramagnetic from diamagnetic motion? In this case, *a priori* knowledge of A for the sample in the absence of MNPs would be needed, and A_{min} would then be defined as a certain number of standard deviations above or below the native A of the medium. This can rapidly become complicated, because A is a function of both magnetization M_m and elastic modulus E_m of the medium, both of which may be spatially varying. Also, assuming the medium is diamagnetic, MNPs at exactly $2\rho_{crit}$ give rise to the same A as without MNPs, and thus would be indistinguishable from control. In this case we could predict a lower bound on ρ_{min} of $2\rho_{crit}$. In essence, we use the mechanical phase filter here because it reduced the need for *a priori* information to a binary question of whether the medium is diamagnetic or not, and, as will be shown empirically below, it greatly improved the sensitivity of our particular MMOCT system, even in highly controlled, spatially homogeneous tissue phantoms.

2.2 Coherence imaging of magnetomotion

Spectral interferometry is used to obtain the complex-analytic time-domain signal $\tilde{S}(\tau)$, which is the mutual coherence function of the electric fields from a reference arm E_R and biological sample E_S (delayed by time τ with respect to one another). $\tilde{S}(\tau)$ is obtained by Fourier transformation $\mathfrak{I}$ of the measured spectral interferogram $S(\omega)$ after background subtraction of the reference field intensity $|E_R(\omega)|^2$ according to the Wiener-Khintchine theorem:

$$\tilde{S}(\tau) = \mathfrak{I}\left\{ S(\omega) - |E_R(\omega)|^2 \right\}, \qquad (8)$$

where ω is the angular frequency of the light and the backscattered intensity from the sample $|E_S(\omega)|^2$ is negligible. For simplicity, the two-dimensional B-mode complex analytic signal is written as $\tilde{S}(x,z)$, where the sample depth $z = \omega\tau / k$ and k is the wave vector in the sample, and the transverse coordinate x is sampled by scanning the beam across the sample. $\tilde{S}(x,z)$ can be written in terms of a slowly-varying envelope S_{env} and relative phase ϕ:

$$\tilde{S}(x,z) = S_{env}(x,z)\exp(i\phi(x,z)). \qquad (9)$$

where S_{env} is a convolution of the point spread function of the OCT system and the sample backscattering amplitude, and $\exp(i\phi)$ is modulated rapidly with half-wavelength periodicity in z.

Mechanically modulated MNPs as described in Eq. (5) will push adjacent light-scattering structures, resulting in a deformation of the tissue that can be measured using phase-resolved OCT. In B-mode imaging this can be accomplished by continuously scanning in x while acquiring rapid axial (z) scans and at the same time modulating the magnetic field in t. However, the axial scans must be sufficiently fast to sample the magnetic field modulation (Nyquist criterion). Also, the magnetomotive signal must be separated from the optical phase changes along the x dimension [22], to allow them to be unmixed. These can be achieved under the following conditions:

$$f_z > 2f_B > \frac{2v}{\Delta x}, \qquad (10)$$

where f_z is the axial (z) line acquisition rate, Δx is the transverse resolution of the OCT system, and v is the velocity of the transverse scan. The latter criterion requires more than one cycle of the magnetic field be completed in the time it takes to transversely scan across one point scatterer.

When scanning is performed in this way, two-dimensional data is acquired where one dimension is z and the other is coupled transverse/temporal (x/t). The complex analytic signal in this case can be written:

$$\tilde{S}(x,z;t) = S_{env}(x,z;t)\exp(i\phi(x,z;t))$$
$$\approx S_{env}(x,z)\exp(i\phi(x,z))\exp(2ik\Delta z(x,z;t)) \qquad for \quad \Delta z \ll l_c \tag{11}$$

where $S_{env}(x,z)$ and $\phi(x,z)$ indicate what would be measured in the absence of magnetomotion. When the displacement Δz is small compared to the coherence length l_c, S_{env} is unchanged and Δz only affects the phase term. Using Eq. (5) the relevant magnetomotive terms are extracted from the B-mode data by computing the complex argument and applying a derivative:

$$D(x,z;t) = \frac{\partial}{\partial t}\left\{\arg\left(\tilde{S}(x,z;t)\right)\right\} = \frac{\partial}{\partial t}\left\{2k\Delta z(x,z;t) + \phi(x,z)\right\}. \tag{12}$$

$$= 2\pi f_B k A(x,z)\cos\left(2\pi f_B t + \varphi(x,z)\right) + \frac{\partial}{\partial t}\phi(x,z)$$

We note that phase unwrapping should be applied during computation of the derivative by taking a modulus 2π. The derivative helps to remove unwanted low frequency noise. Using the latter criterion of Eq. (10), we see that the stationary optical phase term [last term of Eq. (12)] varies more slowly than the magnetomotive term modulated at f_B [first term of Eq. (12)]. This can be shown by Fourier transformation of D along the x/t dimension, as displayed in Fig. 2. A magnetomotive signal proportional to the displacement amplitude $A(x,z)$ can thus be extracted by applying a bandpass filter (BPF) to D in x/t about f_B with an appropriate passband to preserve spatial x variations. The mechanical phase lag $\varphi(x,z)$ is similarly extracted by computing the argument of the bandpass-filtered D.
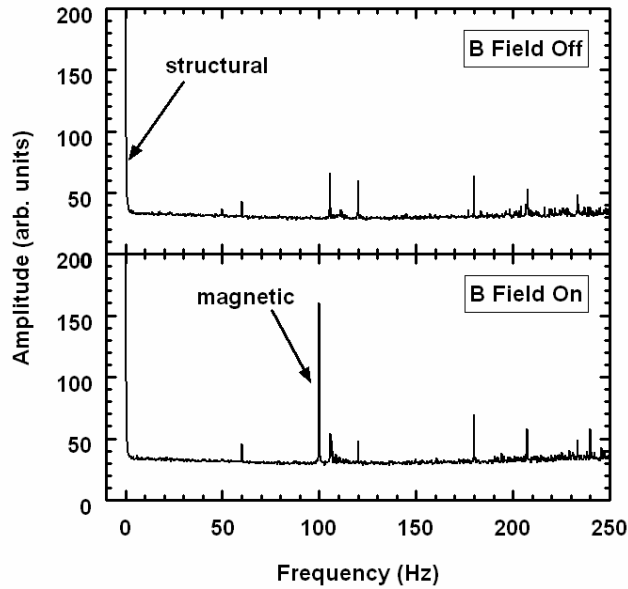

Fig. 2. Representative transverse Fourier spectra with and without magnetic field modulation at 100 Hz for B-mode imaging of a tissue phantom with 100 µg/g MNPs. Spectral amplitudes were averaged over all rows of the image. As indicated, the low frequency peak contains the usual structural OCT data, and a peak at 100 Hz is specific to magnetomotion. Other peaks are attributed to background noise (including 60Hz and its harmonics).

To improve specificity, a B-mode image without magnetomotion should be acquired in the same way to account for physiological motions in the tissue. Thus, we write the background-rejected magnetomotive signal S_{mm} in decibels as follows:

$$S_{mm}(x,z) = 10\log\left(\frac{\hat{f}_{on}(x,z)\big|BPF\{D_{on}(x,z;t)\}\big|}{\hat{f}_{off}(x,z)\big|BPF\{D_{off}(x,z;t)\}\big|}\right), \qquad (13)$$

where D_{on} and D_{off} are the measurements according to Eq. (12) acquired with the magnetic field modulated and off, respectively, and $\hat{f}_{on}$ and $\hat{f}_{off}$ are the mechanical phase filters using Eq. (6) with φ measured from D_{on} and D_{off}, respectively. $S_{mm}(x,z)$ is then displayed directly as the MMOCT image.

We note that this theoretical analysis only treated the case of a homogeneously dispersed MNP-laden tissue. The displacement field $\Delta z(x,z)$ induced by a localized deposit of MNPs is an axially aligned dipole function [23]. The effective resolution of the MMOCT image depends on analysis of the displacement pattern over a relevant area to infer the locations of specific MNP deposits. Given that individual magnetic microparticle-laden cells were resolved in a previous MMOCT study [18], we expect that the resolution of MMOCT will not be prohibitive to imaging in biological samples.

3. Methods

The spectral-domain OCT system consists of a Ti:Al$_2$O$_3$ femtosecond laser (KMLabs, Inc.) producing 800 nm light with a bandwidth of 120 nm (providing l_c ~3 µm axial resolution). This is pumped by 4.5 W of 532 nm light from a frequency-doubled Nd:YVO$_4$ laser (Coherent, Inc.) The broadband light is launched into a single-mode fiber interferometer which is divided into the sample arm and a stationary reference arm. The sample beam is steered using galvanometer mirrors placed one focal length above a 30 mm achromatic imaging lens (providing Δx ~12 µm transverse resolution). A water-jacketed electromagnet described previously [18] is placed between the lens and sample allowing the beam to pass through the central bore. A 250 W power supply is used to achieve a magnetic field of ~0.08 T and gradient of ~15 T/m within the sample imaging volume. The interference of the reference and sample beams is measured with a spectrometer described previously [24], composed of a grating, imaging lens, and line camera (Pirahna 2, Dalsa Inc.) with capability of 33 kHz line rates. The spectrometer resolution was designed to provide an optical imaging depth of 2 mm.

The magnetic modulation frequency f_B was chosen to be 55.6 Hz for tumor tissues and 100 Hz for tissue phantoms, based on the best response (highest A) achieved from these samples. A lower axial scan rate of 1 kHz was chosen to avoid excessive oversampling. The camera exposure time was 250 µs. The root-mean-square phase noise measured from a stationary tissue specimen at 1 kHz without transverse scanning was 0.2 rad. B-mode scans over 2.5 mm were performed with a scan velocity v of 0.625 mm/s, corresponding to a right-hand-term in Eq. (10) of 104 Hz and thus satisfying the criterion for $f_B > 52$ Hz. Each frame consisted of 4000 pixels width by 1024 pixels depth, taking 4 seconds to acquire. Each image was acquired twice, once with the magnetic field modulated and once with the field off, resulting in a total acquisition time of 8 s per MMOCT image. 3-D sampling was performed on each sample by acquiring 6 B-mode images with 0.5 mm spacing in y, resulting in a total imaging area of 2.5×2.5 mm. (The large spacing in y was chosen as a tradeoff between larger sample areas and shorter imaging times.)

MMOCT images were generated according to Eqs. (8), (12), and (13). Initially, the data collected from the line camera is resampled to provide $S(\omega)$ evenly sampled in frequency ω. Median filtering of S_{mm} was performed over 23×23 µm. The bandpass filter width was chosen to pass transverse features of S_{mm} up to a spatial frequency of 1/(32 µm). All images were downsampled by a factor of f_z/f_B along x for portability and cropped to 800 pixels in z to avoid edge effects near the bottom and top of the image. The mean S_{mm} with and without the mechanical phase lag filter $\hat{f}$ were computed for each image. MMOCT images were rendered for display by applying $\hat{f}$ pointwise to S_{mm} at each pixel. Then, for each set of 6

images, the mean and standard deviation of the image-averaged S_{mm} and image-averaged φ were computed. This was all performed in post-processing using a Matlab® script which requires 15 s per image.

Two types of MNPs with similar properties were used (see Fig. 3). The first type, Sigma-Aldrich #637106, are approximately 20-30nm in diameter, composed of pure magnetite (Fe_3O_4) and are without any surface coating. We will refer to these as bare MNPs. These were used for preparation of tissue phantoms because of their miscibility in silicone oils. The second type, Ocean NanoTech #SHP-20, are significantly more monodisperse in size at ~20nm, composed of a combination magnetite/maghemite core (exact ratio unknown) and a polymer coating with a hydrophilic, COOH-terminated outer surface. We will refer to these as COOH-MNPs. These are stable in aqueous solutions (including saline solutions), and were used for the tissue imaging study.

Transmission electron microscopy (Philips CM200, FEI Company) was performed on each type of MNP for sizing. SQUID (superconducting quantum interference device) magnetometry (1T MPMS, Quantum Design, Inc.) showed the bare MNPs exhibited a volume magnetic susceptibility $\chi = 4.1$, saturation magnetization $M_{sat} = 93$ emu/g Fe, and remanence of 7 emu/g Fe. In comparison, the COOH-MNPs exhibited a $\chi = 2.5$, $M_{sat} = 105$ emu/g Fe, and remanence of 0.3 emu/g Fe. We expect the coercive field to be small because the MNPs are on the order of a single domain size; lacking significant remanence, they can be approximated as superparamagnetic. Inductively-coupled plasma mass spectrometry (OES Optima 200 DV, Perkin Elmer) revealed that, due to their polymer coating, the COOH-MNPs consist of 34% Fe by weight, compared to 72% Fe for the bare MNPs.
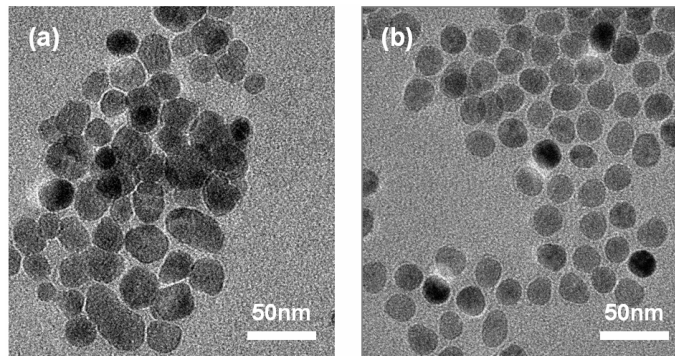

Fig. 3. Transmission electron micrographs of MNPs. (a) 20-30nm bare MNPs. (b) 20nm COOH-terminated MNPs.

Silicone tissue phantoms which have comparable optical and mechanical properties to tissue were prepared exactly in the same way as reported previously [18], except we note a typographical error in [18] where the concentration of TiO_2 used is actually 4 mg/g. Briefly, a mixture of crosslinking and non-crosslinking polymers is used to provide a tissue-like viscoelastic medium, and TiO_2 microparticles are added to qualitatively match the OCT signal achieved from 2% intralipid (~40 cm^{-1} scattering coefficient). Varying concentrations of bare MNPs are added and the samples are homogenized via sonication before crosslinking in an oven. SQUID magnetometry was also performed on the tissue phantom medium without added MNPs, resulting in a measured magnetic susceptibility of $\chi = 6\times10^{-6}$. In comparison, human tissues are known to have a susceptibility typically within 20% of that of pure water, $\chi = 9\times10^{-6}$ [1].

Mammary tumors were induced in a Wistar-Furth female inbred rat (The Jackson Laboratory, Bar Harbor, ME) via intraperitoneal injection of a carcinogen (N-methyl-N-nitrosourea) according to a protocol described in detail previously [25]. After euthanasia, a tumor of $1.4 \times 1.6 \times 0.6$ cm dimensions was harvested from the right groin area and stored at

-80°C before imaging. MMOCT imaging was performed immediately after thawing the tumor. The tumor was subsequently immersed in a saline solution with ~4 mg/g COOH-MNPs for 15 minutes at room temperature, rinsed vigorously in pure saline for ~1 minute, and imaged using MMOCT. (The relatively large MNP concentration was chosen to ensure positive results for this single tumor). Again, the tumor was immersed in the MNP solution and the process of rinsing and imaging repeated to collect data for cumulative immersion times of 30, 60, 90, and 120 minutes. Every effort was made to image the same tumor surface area, however, exact registration between successive images was not maintained.

4. Results and discussion

4.1 MMOCT imaging of tissue phantoms

MMOCT imaging was performed on silicone phantoms with tissue-like optical and mechanical properties to understand the sensitivity to small MNP doses. The numerical results are plotted in Fig. 4. The mechanical phase lag φ for the control is 2.3 radians, compared to -0.4 radians for the most heavily dosed sample. There appears to be a small negative bias in φ which might be due to the viscosity in the medium; however, the overall difference between the positive and negative control phantoms is 2.7 which is near the expected value π. At 15 µg/g the mechanical phase appears to be approximately halfway between these two extremes, suggesting that this concentration is very near ρ_{crit} [Eq. (3)] where the forces between the diamagnetism of the sample are balanced by those from the paramagnetic MNPs. In fact, this is in good agreement with the predicted value of ρ_{crit}=12 µg/g (Fig. 1) for this experiment where B=800 G.
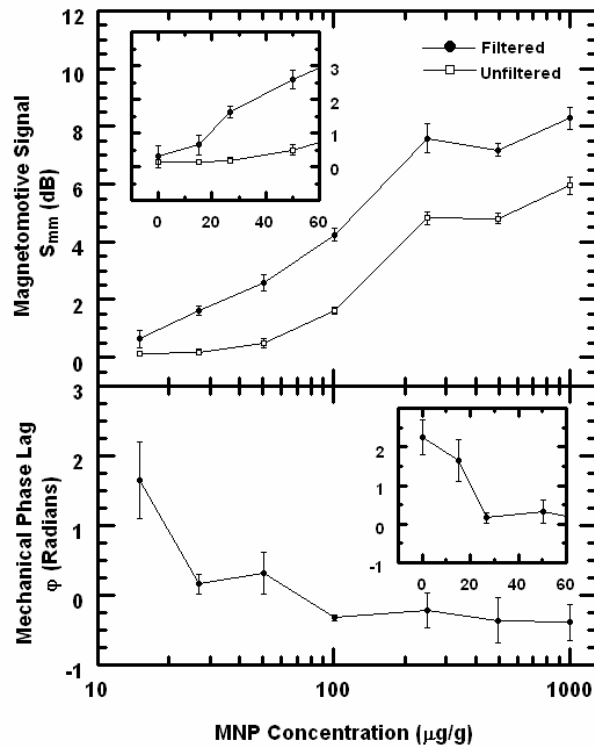

Fig. 4. Plots of MMOCT signals in silicone tissue phantoms vs. MNP concentration. Top panel: Magnetomotive signal S_{mm} is shown with and without the mechanical phase lag filter [Eq. (13)]. Top inset: Data near zero concentration is shown on a linear scale. Bottom panel: Mechanical phase lag φ is plotted. Bottom inset: Data near zero concentration is shown on a linear scale.

We see in Fig. 4 that the use of the mechanical phase lag filter [Eq. (6)] to differentiate paramagnetic motion from diamagnetic motion allows for the 27 µg/g phantom to be distinguished from control by more than one standard deviation, compared to 50 µg/g when the filter is not used. This is because the diamagnetic control sample motion exhibits a significant nonzero displacement amplitude A, and without measuring the mechanical phase φ, it cannot be distinguished from that from the 27 µg/g phantom.

If we use this result to estimate ρ_{min}=27 µg/g, and assuming ρ_{crit}=12 µg/g based on the SQUID magnetometry, we can then estimate ρ_{noise} =15 µg/g for our field strength of 800 G. Using this result to scale the theoretical curve of $\rho_{noise}(B)$ appropriately in Fig. 1 allows us to predict $\rho_{min}(B)$ for all B, and we find that the minimum value of ρ_{min} =26 µg/g is arrived at B=1000G. Therefore, we expect that our present setup with ρ_{min} =27 µg/g at 800 G is very close to the optimum sensitivity. This optimization is specific to the hardware noise of the OCT system, the magnetizations of the MNPs and sample, and the mechanical properties of the sample.

We note that S_{mm} begins to level for MNP concentrations above 250 µg/g. This occurs because the displacement amplitude becomes large, and the optical phase changes by more than π between successive samples. This situation can be written as:

$$2k\frac{\partial}{\partial t}\Delta z > \pi f_z .\qquad(14)$$

And thus, in this case, one cannot properly unwrap the optical phase to track the magnetomotion. This problem can be mitigated by increasing the line rate f_z, which allows MMOCT to sense a higher dynamic range of MNP concentrations.

The OCT and MMOCT images from these tissue phantoms are shown in Fig. 5. We see that, while the OCT images are indistinguishable, the MMOCT images clearly show the expected dependence on MNP concentration. A few interesting effects can be noted. First, observe the autocorrelation artifact in the upper portion of the OCT images, which is due to non-negligible $|E_S|^2$ for these strongly scattering phantoms. Interestingly, this artifact is absent from the MMOCT images. This is because the $|E_S|^2$ term has no optical phase; only the $E_S^*E_R$ interference term carries the relative optical phase between the reference and sample electric fields. Since the MMOCT algorithm measures modulation in the optical phase to deduce the sample displacement, we expect it to be insensitive to the autocorrelation artifact. In fact, this is very similar to standard techniques currently employed to eliminate autocorrelations through phase modulation [26].

Secondly, we observe that the MMOCT images are not attenuated in z as rapidly as the OCT images. This is because the average value of the optical phase is independent of the scattering intensity, depending only on the amplitude of magnetomotion which is relatively independent of depth for homogeneous samples much thicker than the imaging depth. The phase noise, however, does increase with decreasing scattering intensity [19], and thus we find the MMOCT signal eventually becomes noisy at a depth where the scattering intensity is sufficiently low. The fact that the average MMOCT signal is relatively depth-independent is an improvement from the previously reported amplitude-based MMOCT methods where the scattering intensity scales the MMOCT contrast [17,18].
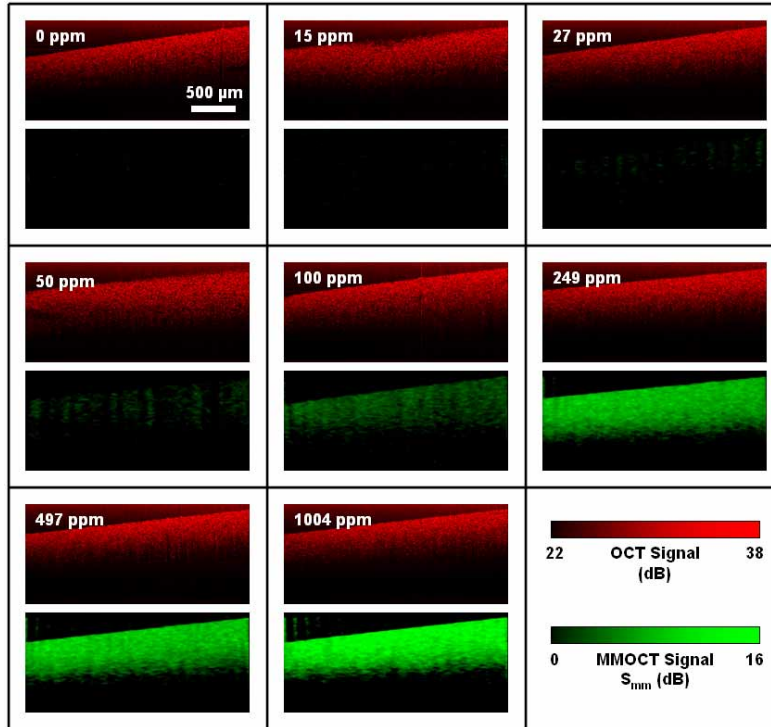
Fig. 5. Representative OCT and MMOCT images of tissue phantoms with varying concentrations of magnetic nanoparticles (1 ppm = 1 µg/g), corresponding to the data of Fig. 4. Within each box, the upper panel is the OCT image in red, and the lower panel is the corresponding MMOCT image in green.

4.2 MMOCT imaging of tissues

To learn whether these techniques are relevant to imaging MNPs in real biological tissues, we studied the diffusion of MNPs into an excised rat tumor over a 2 hour period. The MMOCT signals versus diffusion time are displayed in Fig. 6. The mechanical phase lag φ before introduction of the MNPs is -2.2 which is near $\pm\pi$, indicative of a diamagnetic response from the tumor. After MNPs diffused into the tumor for only 15 minutes, φ shifted toward zero, indicating that the MNPs were of sufficient concentration to result in a net paramagnetic response. The magnetomotive signal S_{mm} showed a rapid increase over 1 hour, after which it leveled off. The leveling could be due to two effects: 1) the concentration of MNPs reached a steady state in the tissue, and/or 2) the MNP concentration was above the available dynamic range of S_{mm}. Since 4 mg/g is significantly above the concentration at which S_{mm} leveled in tissue phantoms (Fig. 4), we expect the latter effect cannot be neglected.
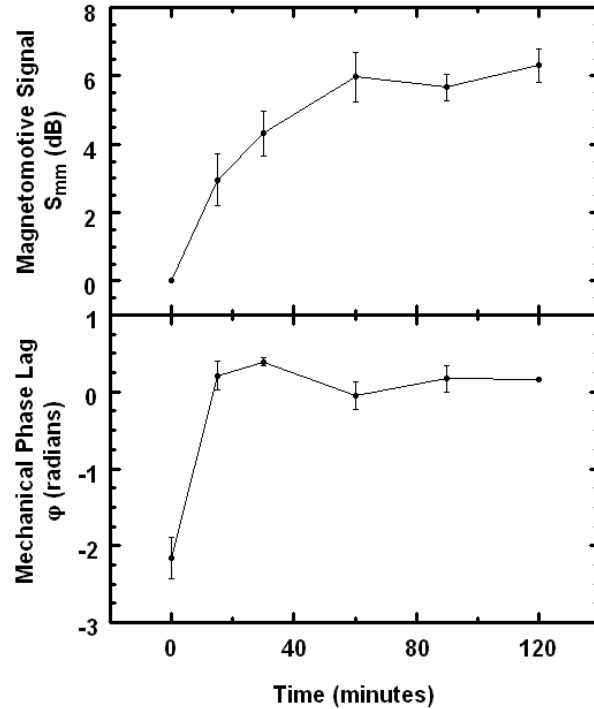
Fig. 6. Plots of MMOCT signals in an excised rat tumor vs. diffusion time of MNPs. Top panel: Magnetomotive signal S_{mm} computed according to Eq. (13). Bottom panel: Mechanical phase lag φ.

The overlaid OCT and MMOCT images of the tumor during diffusion of MNPs is shown in Fig. 7. Although the S_{mm} at longer time periods leveled, the MMOCT images exhibit a useful dynamic range of approximately 16 dB. There appears to be structure in the MMOCT image correlated with the structure in the OCT image, which may be liquid voids. We note that MNPs in liquid phantoms do not exhibit MMOCT contrast for two reasons: 1) their motion is not constrained and upon application of the field the MNPs move continuously along magnetic field gradients, and 2) their Brownian motion is too fast compared to the sampling rate, which results in decorrelation of the optical phase.

We also note that, while there is some transverse variation in the MMOCT signals, such as in the 15 and 60 minute images, there is no depth-dependent gradient that one might expect to observe during a diffusion process. This may be because the diffusion length at ≥ 15 minutes is much longer than the imaging depths of ~600 µm achieved in this tumor. However, further investigation is needed to understand on what length scale the magnetomotion is mechanically coupled within the tissue, which will determine the spatial resolution of MMOCT imaging.
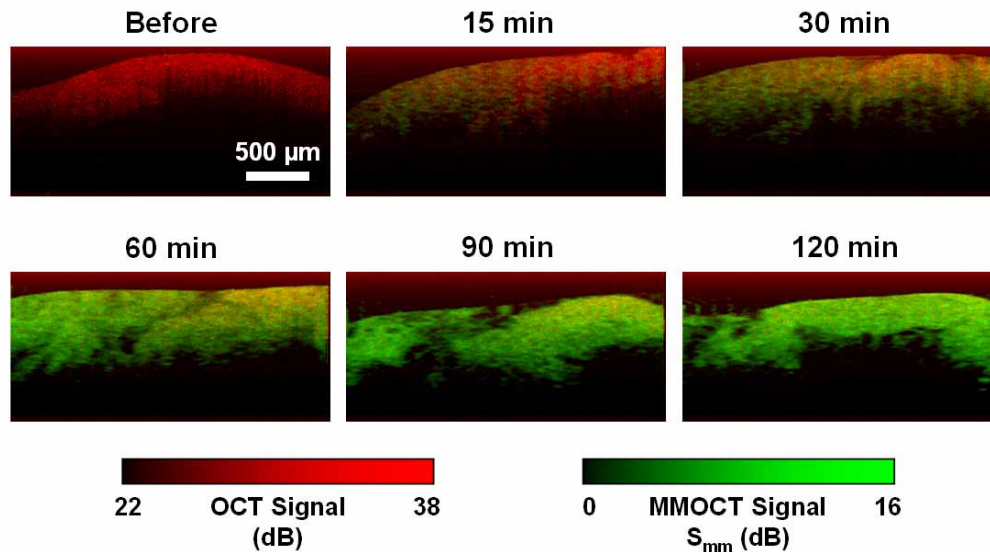
Fig. 7. Representative MMOCT images of MNP diffusion in tumors versus time. Red and green display the structural (OCT) and magnetomotive (MMOCT) image channels, respectively, as indicated by the colored scale bars.

5. Summary

In this work we present a new MMOCT imaging system based on phase-resolved detection of magnetic nanoparticle displacements, with improved sensitivity to 27 µg/g of MNPs from previously reported 450 µg/g [18] for an amplitude-based MMOCT system. The speed of imaging is improved from 60 s for a 0.6 mm B-mode scan to 8 s for a 2.5 mm scan, a factor of over 30 times faster. This is accomplished by continuously modulating the magnetic field with a square-root sinusoid to produce a pure sinusoidal force on the MNPs. The fundamental limit of imaging speed may be limited by the tissue mechanics; in this experiment we found tumor tissues had a larger mechanical response at 56 Hz than at 100 Hz. We found that the optical scattering and magnetomotive signals could be separated into two frequency channels for B-mode imaging by appropriate choice of the transverse scanning speed and magnetic modulation frequency f_B.

We note that the phase sensitivity of our MMOCT system is relatively poor with 0.2 rad phase noise at 1 kHz. However, recent experiments suggest that the optical phase sensitivity may be practically limited to ~0.1 rad for *in vivo* applications [27], and thus, the phase sensitivity of our system may not be a significant limiting factor.

The use of a mechanical phase filter to resolve paramagnetic from diamagnetic samples was crucial for achieving the highest sensitivity to the MNPs. In tissue phantoms, we found the mechanical phase lag shifted predictably from near π at zero MNP concentration (diamagnetic) to near 0 at high MNP concentration (paramagnetic). We found that a late stage rat mammary tumor exhibited a diamagnetic response, which then shifted to paramagnetic after soaking in MNPs. While our method requires *a priori* knowledge that the tissues are diamagnetic, experience shows that human tissues are diamagnetic, typically lying within 20% of the susceptibility of H_2O [1].

Theoretical analysis showed that an optimum magnetic field strength balanced the effects of saturation of MNPs at high fields with too little magnetomotive force at low fields. For our experiments we predict the optimum B ~1000 G, which was very close to our applied field of 800 G. To the degree that the biological phantoms, MNPs, and OCT system were typical, we expect that the choice of magnetic fields in this strength range will generally yield the best results.

6. Conclusion

MMOCT imaging provides a new way of tracking MNPs on the microscale. With the additional speed and sensitivity afforded by this new MMOCT system, we have demonstrated imaging of diffusing MNPs in an excised rat mammary tumor model. We found that MNPs rapidly diffuse into an excised tumor over a time scale of < 15 minutes, and MMOCT images exhibited a dynamic range of ~16 dB. The toxicity of these MNPs during topical administration is not known, however, the concentration of MNPs needed to track MNP diffusion may be considerably lower than the 4 mg/g used in this study.

The enhanced MNP sensitivity of 27 µg/g or ~2 nM corresponds to ~600 MNPs per 10 µm diameter cell volume. This will be useful for tracking functionalized MNPs targeted to cellular receptors. A recent *in vivo* mouse experiment suggests that it is possible to target hundreds of nM of MNPs to cancer [6], therefore the MMOCT MNP sensitivity may be useful for *in vivo* molecular imaging. While safety of the MNPs in this study has not been investigated, similar iron oxide MNPs with a dextran coating are in clinical use as MR contrast agents (Feridex I.V., Advanced Magnetics, Inc.), which are administered intravenously at a dose of 0.56 mg Fe/kg. MMOCT may facilitate the development of MNPs for biomedical applications such as hyperthermic therapy, and provide molecular contrast in OCT imaging.